INTERNATIONAL JOURNAL FOR NUMERICAL METHODS IN FLUIDS, VOL. 20, 307–318 (1995)

NUMERICAL CALCULATIONS OF THREE-DIMENSIONAL TURBULENT VORTEX BREAKDOWN

ROBERT E. SPALL

Department of Mechanical Engineering, EGCB 212, University of South Alabama, Mobile, AL 36688, U.S.A.

AND

THOMAS B. GATSKI

Theoretical Flow Physics Branch, MS 156, NASA Langley Research Center, Hampton, VA 23681, U.S.A.

SUMMARY

Numerical solutions to the three-dimensional, unsteady, incompressible Reynolds-averaged Navier–Stokes equations have been obtained for bubble-type vortex breakdown. Two different turbulence models were employed: (1) standard K–ε and (2) an explicit, regularized algebraic Reynolds stress model. Results are computed at a Reynolds number of 10,000. The algebraic Reynolds stress model produced a breakdown bubble with a larger length-to-diameter ratio than did the K–ε model. Breakdown also occurred at lower levels of adverse pressure gradient for the algebraic stress model than for the K–ε model. In each case single-cell breakdown structures resulted. This is contrasted with numerical calculations for laminar breakdown which reveal the existence of complex multicell bubble breakdown structures.

KEY WORDS vortex breakdown; turbulence; computational fluid dynamics

1. INTRODUCTION

The vortex breakdown phenomenon has been widely studied. This is due in part to important technological applications of vortex breakdown. For instance, breakdown has been proposed as a possible mechanism for accelerating the destruction of wing tip vortices, which may limit aircraft traffic at major airports. Breakdown is also an important consideration for fighter-type aircraft, in that the handling characteristics of the aircraft may be drastically altered owing to the occurrence of breakdown. These problems have provided strong motivation for the study of breakdown by the aerodynamics community. An additional application of breakdown is in the area of combustion. Here the breakdown acts as a fluid dynamic flame holder, serving to stabilize the flame and to recirculate hot gases within the combustor primary region.[1]

Although the above-mentioned applications invariably involve turbulent flows, owing to the complexity of the problem, theoretical studies have emphasized the laminar case. However, after 35 years of study no consensus regarding the physical mechanism responsible for the initiation of breakdown exists. The sheer volume of work prohibits an extended discussion here. The reader is referred to comprehensive reviews by Hall[2] and Leibovich.[3]

CCC 0271–2091/95/040307–12

Received 20 October 1993
Revised 28 February 1994

As with the theoretical studies, the majority of the experimental works have considered laminar vortex breakdown. The primary experimental tool has been flow visualization for breakdown occurring within straight or slightly diverging tubes[4,5] or over delta wings.[6] Additional studies have utilized LDV[7] or PTV[8] measurements to provide information concerning the internal structure of bubble- and spiral-type breakdowns. These (and other) works reveal that as many as seven distinct types of laminar breakdown exist, although the most commonly observed are the spiral and bubble forms. Unfortunately, experimental results under high-Reynolds-number turbulent flow conditions performed in similar tube-and-vane-type experimental apparatus are not available. However, a large number of experimental studies from the combustion community exist concerning the occurrence of breakdown for swirling flows subject to a sudden expansion.[9–11] These flows are intended to be representative of the (cold flow) turbulent, swirling flows generated within prototypical gas turbine can-type combustion chambers.

The majority of the numerical works concerning vortex breakdown have concentrated on low-Reynolds-number, laminar, axisymmetric[12,13] or three-dimensional[14–19] flows. Recent results for laminar three-dimensional vortex breakdown[17] provide details regarding the structure of four distinct forms of breakdown—helical, double-helix, spiral and bubble type. These results were further presented in video format in Reference 20. Thus a primary contribution of the numerical works has been to reveal details of the internal structure of the various forms of breakdown.

Numerical calculations for turbulent vortex breakdown (or breakdown-like-flows) have been motivated by applications in gas turbine combustion. Here the structure of the breakdown is of considerable importance and the accuracy of the turbulence models is consequently an important issue. Representative work includes that of References 21–23. In these studies either K–ε or differential Reynolds stress models were employed. The combustor geometry and associated flow fields may become quite complex, especially when features such as dilution jets are considered.[24]

In the present work we consider the effect of turbulence on vortex breakdown, isolated from the complicating factors considered in previous combustor-related studies. Numerical solutions for turbulent, three-dimensional, bubble-type breakdown in an unbounded domain subject to a decelerating freestream axial velocity are obtained. It is well known that linear two-equation models do not inherently contain a mechanism capable of capturing the sensitivity of turbulence stresses to swirl-induced body forces. Second-order Reynolds stress closures (either algebraic or differential) represent the lowest level of closure which inherently accounts for these effects. Thus results are computed using two separate turbulence models: (1) a linear K–ε model and (2) a recently developed explicit, regularized algebraic Reynolds stress model.[25] For comparative purposes, results are also presented for laminar breakdown at a Reynolds number of 200. The algorithm is an extension of that used in the authors' previous studies of vortex breakdown[16,17] to include the effects of turbulence.

2. NUMERICAL METHOD

The three-dimensional incompressible Reynolds-averaged Navier–Stokes equations are solved numerically using the second-order-accurate (in time and space) velocity–vorticity formulation of Gatski *et al.*[26] The non-dimensional governing equations in terms of mean velocity, $\bar{u} = \bar{u}(\bar{x}, t)$, and mean vorticity, $\bar{\zeta} = \bar{\zeta}(\bar{x}, t)$, variables are given by

$$\nabla \cdot \bar{u} = 0, \tag{1a}$$

$$\nabla \times \bar{u} = Ro^{-1}\bar{\zeta}, \tag{1b}$$

$$\frac{\partial \bar{\zeta}}{\partial t} + (\bar{u} \cdot \nabla)\bar{\zeta} = (\bar{\zeta} \cdot \nabla)\bar{u} + Re^{-1}\nabla^2\bar{\zeta} = \nabla \times (\nabla \cdot \tau_{ij}), \tag{2a}$$

$$\nabla \cdot \bar{\zeta} = 0. \tag{2b}$$

Velocities have been non-dimensionalized by the freestream velocity and vorticities have been non-dimensionalized by Ω, defined as the solid body rotation rate obtained from $\Omega = \lim_{r \to 0}(V_\theta/r)$. The length scale l is taken as the vortex core radius at inflow. In addition, Re is the Reynolds number (Ul/ν) and Ro is the Rossby number defined as $U/l\Omega$. The Reynolds stresses are represented by τ_{ij}. Since the process of time averaging has introduced additional unknowns, additional equations must be introduced to close the system. In the present work two different closures are considered: (1) a standard K–ε model and (2) a regularized algebraic Reynolds stress model (ARSM).[25]

For the K–ε model the Reynolds stresses are expressed in terms of the mean velocity gradients as

$$\tau_{ij} = \tfrac{2}{3}K\delta_{ij} - 2\nu_t\bar{S}_{ij}, \tag{3}$$

where $\bar{S}_{ij}$ is the rate-of-shear tensor, $\nu_t = C_\mu K^2/\varepsilon$ is the turbulent viscosity and K is the turbulence kinetic energy.

The derivation of algebraic Reynolds stress models is based on a production-equals-dissipation equilibrium hypothesis in which Reynolds stress convective and transport effects may be neglected. While previous algebraic models have been implicit in nature, the model used herein is explicit. In addition, the model is regularized so that it remains well-behaved even in the presence of large strain rates. The algebraic Reynolds stress model is written in the form[25]

$$\tau_{ij} = \tfrac{2}{3}K\delta_{ij} - \frac{6(1+\eta^2)\alpha_1 K}{3+\eta^2+6\zeta^2\eta^2+6\zeta^2}\left[S^\circ_{ij} + \left(S^\circ_{ik}W^\circ_{kj} + S^\circ_{jk}W^\circ_{ki}\right) - 2\left(S^\circ_{ik}S^\circ_{kj} - \tfrac{1}{3}S^\circ_{kl}S^\circ_{kl}\delta_{ij}\right)\right], \tag{4}$$

where $\alpha_1 = (C_2 - \frac{4}{3})/(C_3 - 2)$ and S°, W°, η and ζ are defined as

$$S^\circ_{ij} = \tfrac{1}{2}g\bar{\tau}(2 - C_3)\bar{S}_{ij}, \tag{5}$$

$$W^\circ_{ij} = \tfrac{1}{2}g\bar{\tau}(2 - C_4)\bar{\omega}_{ij}, \tag{6}$$

$$\eta_{ij} = \left(S^\circ_{ij}S^\circ_{ij}\right)^{1/2}, \tag{7}$$

$$\zeta_{ij} = \left(W^\circ_{ij}W^\circ_{ij}\right)^{1/2}. \tag{8}$$

Here $\bar{\omega}_{ij}$ is the rate-of-rotation tensor and $\bar{\tau} = K/\varepsilon$. Values of $C_2 = 0{\cdot}36$, $C_3 = 1{\cdot}25$, $C_4 = 0{\cdot}40$ and $g = 0{\cdot}233$ have been assigned to the constants. These values were chosen to provide consistency with the second-order closure of Speziale *et al.*[27] Note that the ARSM formally constitutes a two-equation turbulence model, equivalent to the K–ε model when (4) is linearized with respect to the mean velocity gradients. (In this case $C_\mu = 0{\cdot}113$.)

For each model the distributions of turbulence kinetic energy and turbulence dissipation rate are required and are obtained by solving the following general forms of modelled transport equations for K and ε:

$$\frac{DK}{Dt} = -\tau_{ij}\frac{\partial v_i}{\partial x_j} - \varepsilon + \frac{\partial}{\partial x_i}\left(\frac{\nu_t}{\sigma_K}\frac{\partial K}{\partial x_i}\right), \tag{9}$$

$$\frac{D\varepsilon}{Dt} = -C_{\varepsilon 1}\frac{\varepsilon}{K}\tau_{ij}\frac{\partial v_i}{\partial x_j} - C_{\varepsilon 2}\frac{\varepsilon^2}{K} + \frac{\partial}{\partial x_i}\left(\frac{\nu_t}{\sigma_\varepsilon}\frac{\partial \varepsilon}{\partial x_i}\right), \tag{10}$$

where $\nu_t = C_\mu K^2/\varepsilon$, $C_\mu = 0{\cdot}09$, $\sigma_K = 1{\cdot}0$, $\sigma_\varepsilon = 1{\cdot}3$ and $C_{\varepsilon 1} = 1{\cdot}44$. In addition, $C_{\varepsilon 2} = 1{\cdot}83$ for the ARSM, while $C_{\varepsilon 2} = 1{\cdot}92$ for the K–ε model.

A brief discussion of the solution procedure follows. The method is fully described in Reference 26. The div–curl equations form the basis of the solution of the velocity vector, given the vorticity vector at time n, along with the velocity boundary conditions. The vorticity is advanced from time level n to $n + 1$ using (2*a*). The solenoidal condition on the vorticity (2*b*) is enforced to ensure that the initial solenoidal vorticity field (which may be contaminated owing to round-off errors, truncation errors or errors introduced through outflow boundary conditions) remains solenoidal for all time. The computational domain is divided into a region of rectangular elements. Velocities, which are required at the centres of cell faces, are averages of box variables defined at the vertices of each element. Vorticity is also defined at the centres of element faces and represents an average value over a face.

Using the initial distribution of vorticity, the computational sequence is begun by computing the velocity field at time level n utilizing the div–curl equations. The equations are solved subject to the specification of one velocity component on each face of the boundary. The numerical scheme for solving the vorticity transport equation involves a transformation of the vorticity variable

$$\bar{\zeta} = \exp\left[\bar{b}(t - t_n)\right]\bar{\xi}, \tag{11}$$

where

$$\bar{b} = \tfrac{1}{2}\nabla\left(\bar{u} + \bar{u}^T\right) \tag{12}$$

The resulting transport equation for $\bar{\xi}$ takes the form

$$\frac{\partial \bar{\xi}}{\partial t} + \bar{u}\cdot\nabla\bar{\xi} = Re^{-1}\nabla^2\bar{\xi} - \nabla\times\nabla\cdot\tau_{ij}. \tag{13}$$

The effect of the transformation is to uncouple the components of the pseudovorticity $\bar{\xi}$ in the transport equation. Note that the coupling of the components of the vorticity $\bar{\zeta}$ remains intact, since the solution is advanced in time using (3a), although at time level n, $\bar{\xi} = \bar{\zeta}$. The vorticity is advanced to time level $n + 1$ using the velocities at time level n and appropriate vorticity boundary conditions. In the specification of these boundary conditions all components of vorticity are specified at the boundary surfaces. The computed vorticity is then projected onto a new vector space which satisfies the requirement that the vorticity vector is solenoidal. The transport equations for K and ε are solved in a similar manner (although no solenoidal condition need be satisfied).

3. INITIAL AND BOUNDARY CONDITIONS

The specification of initial and boundary conditions for the velocity and vorticity vectors follows from the earlier work of Spall *et al.*[16] and Spall and Gatski.[17] Briefly, the initial conditions are represented by a Burgers vortex, which in non-dimensional form is given by

$$v_\theta = Ro^{-1}\left(1 - e^{-r^2}\right)/r. \tag{14}$$

The vorticity boundary conditions are derived in part from (14). The radial boundaries are sufficiently displaced from the vortex core such that the flow is irrotational and thus the mean vorticity at these boundaries is set to zero. At outflow Dirichlet-type conditions on vorticity are obtained from the inviscid vorticity transport equation. In the calculations to be presented, the Rossby number was set to the supercritical value of 0·9. Consequently, at the radial boundaries a decelerating axial velocity is

specified. This specification drives the vortex from supercritical to subcritical at some location sufficiently far downstream from the inflow boundary. A hyperbolic tangent function was utilized in this study. This is in contrast with the authors' previous works[16,17] on laminar breakdown in which a linear deceleration was employed. It was found that the hyperbolic tangent function provided a superior means of fixing the axial location of the breakdown within the domain.

Owing to a lack of experimental data, specification of the boundary conditions for turbulence kinetic energy and dissipation rate is somewhat subjective. Chiger and Corsiglia,[28] in wind tunnel studies of vortices formed by rectangular wings, indicate extremely low levels of turbulence outside the vortex core, increasing to reach a maximum at or near the vortex centreline. Consistent with this structure and following Bilanin *et al.*,[29] we employ a Gaussian-like distribution for the turbulence kinetic energy at the inflow boundary. This distribution is also utilized to specify the initial conditions. The dissipation rate is specified, through scaling arguments, as $\varepsilon = K^{3/2}/l$, where l is taken as the vortex core radius at inflow. The complete set of boundary conditions is summarized in Table I.

The discretized governing equations were solved over a $75 \times 42 \times 42$ grid (74 cells in the x-direction, 41 cells each in the y- and z-directions). The domain was bounded by $0 \leqslant x \leqslant 40$, $0 \leqslant y \leqslant 20$ and $0 \leqslant z \leqslant 20$. The vortex was positioned in the y–z plane so that the initial vortex centreline was at $y = z = 10$. Based upon a comparison of the results for the laminar calculation with the authors' previous results[16,17] and owing to the fact that the structure of the turbulent breakdown is

Table I. Summary of boundary conditions

	Div–curl equations
Inflow	$u = 1$
Outflow	$\partial v/\partial y + \partial w/\partial z = 0$
Radial boundaries	$u = 1 - \delta\{1 + \tanh [0{\cdot}25(x - 15)]\}$
	Vorticity transport equation
Inflow	$\zeta_x = 2 \exp\left\{-\left[(y - y_c)^2 + (z - z_c)^2\right]\right\}$
	$\zeta_y = Ro\ (\partial u/\partial z - \partial w/\partial x)$
	$\zeta_z = Ro\ (\partial v/\partial x - \partial u/\partial y)$
Outflow	$\mathrm{D}\bar{\zeta}/\mathrm{D}t = \bar{u} \cdot \nabla\bar{\zeta}$
Radial boundaries	$\bar{\zeta} = 0$
	Turbulence kinetic energy
Inflow	$K = 0{\cdot}01 + 0{\cdot}09 \exp\left\{-\left[(y - y_c)^2 + (z - z_c)^2\right]\right\}$
Outflow	$\mathrm{D}K/\mathrm{D}t = \bar{u} \cdot \nabla K$
Radial boundaries	$K = 0{\cdot}01$
	Dissipation rate
Inflow	$\varepsilon = K^{3/2}/l$
Outflow	$\mathrm{D}\varepsilon/\mathrm{D}t = \bar{u} \cdot \nabla\varepsilon$
Radial boundaries	$\varepsilon = K^{3/2}/l$

simpler than that of the laminar case (a single recirculation region versus multiple recirculation cells), this resolution was deemed sufficient. The scheme is implicit, so there are no numerical constraints on the size of the time step Δt. Thus a time step of 0·2 was used throughout the simulation to march to a quasi-steady state. Numerical experimentation with $\Delta t = 0{\cdot}1$ revealed no significant changes in the solution.

4. RESULTS

Results are presented and compared for bubble-type breakdown using both the algebraic Reynolds stress model and a K–ε model. In each case the Reynolds number based on the vortex core radius at inflow and freestream axial velocity was 10,000. The results presented represent quasi-steady state solutions, i.e. no significant changes in the structure of the bubbles occurred as time evolved. For comparative purposes, laminar breakdown calculations at a Reynolds number of 200 are also presented. In the figures to follow, the results are presented on the plane $z = 10$ (i.e. along the vortex centreline).

Some difficulties in making direct comparisons between results obtained using the different turbulence models arose owing to the sensitivity of the breakdown process to the parameter δ (used to fix the freestream velocity distribution; see Table I). Results revealed that breakdown for the algebraic stress model was obtained for $\delta = 0{\cdot}13$, while for the K–ε model $\delta = 0{\cdot}21$. Note that these are the approximate minimum values for bubble-type breakdown to occur for each of the models. Larger values produced bubbles of similar shape that grew rapidly, eventually interfering with the lateral boundary conditions. Thus it was felt that the most meaningful calculations were obtained by using the approximate minimum value of δ required for breakdown to occur. We note, however, that Spall *et al.*[30] compiled results for a large number of experimental and numerical breakdown flow fields which highlighted the sensitivity of the process to swirl levels when the nominal Reynolds number is below 100. Thus, considering the dissipative nature of the K–ε turbulence model under swirling flow conditions, this behaviour is not unexpected.

Streamlines/velocity vectors for the ARSM and K–ε models are shown in Figures 1(a) and 1(b) respectively. These figures indicate that each bubble consists of a single toroidal recirculation zone. This is in contrast with the laminar numerical results of Spall *et al.*,[16] and the laminar experimental results of Faler and Leibovich[7] in which the forward portion of the bubble contained one or more additional toroidal recirculation zones. However, the primary difference between the results of the two turbulence models lies in the overall shape (or envelope) of the bubble. The length/diameter (L/D) ratio of the bubble produced using the ARSM is approximately 3·25, while for the K–ε model $L/D = 2{\cdot}25$. Thus the ARM model produces a longer, more slender breakdown region. This is in accord with the observation that linear two-equation models tend to underpredict the length of recirculation zones in the standard backward-facing step calculation and indeed for swirling, recirculating flows in general.[22] Thus, although experimental data are not available, the present results are consistent with previous numerical calculations for related (confined) flow fields.

Shown in Figure 1(c) are velocity vectors resulting from laminar calculations with the parameter $\delta = 0{\cdot}13$. Note the existence of a more complicated multicell breakdown structure (similar to the authors' previous results[16,17] for which a more detailed analysis is presented). The fluid in the forward portion of the bubble is quite quiescent, with the primary toroidal vortex appearing in the aft portion of the bubble. Compared with the turbulent cases, one also notes that the overall size of the bubble is somewhat diminished and that the initial stagnation point occurs further upstream. The size differences may be due to the fact that the laminar bubble is situated upstream of the region ($14 < x < 18$) over which the axial velocity deceleration takes place along the lateral boundaries. Therefore the laminar and turbulent bubbles are subjected to different (large radius) potential flow solutions and one might

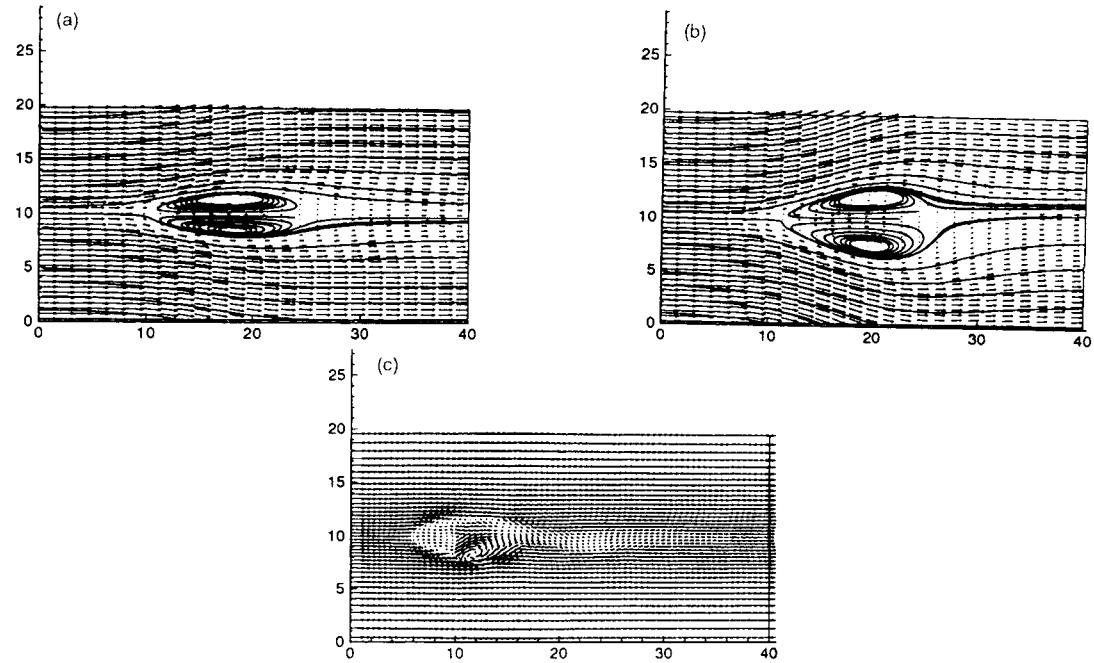

Figure 1. Streamlines and velocity vectors for vortex breakdown (along vortex centreline): (a) ARSM (Re = 10,000, δ = 0·13); (b) K–ε model (Re = 10,000, δ = 0·21); (c) laminar breakdown (Re = 200, δ = 0·13)

expect that a bubble situated in a region of strong adverse pressure gradient would be larger than one located in a region where the adverse gradient was diminished. Thus this figure serves to highlight some of the primary differences between laminar and turbulent numerical calculations of vortex breakdown (subject to the given boundary conditions).

In Figure 2 we present contours of mean axial velocity for the ARSM. The effects of the freestream deceleration are indicated via the contour lines intersecting with the lateral boundaries between x = 14 and 18. This deceleration acts to centre the bubble in the computational domain, minimizing contamination problems with inflow and outflow boundary conditions. Here the initial stagnation point is located approximately 10 core radii downstream from the inflow boundary. It is also revealed that the bubble is nearly symmetric about the original vortex centreline and that the magnitude of the maximum reversed velocity within the bubble is approximately 10% of the freestream axial velocity.

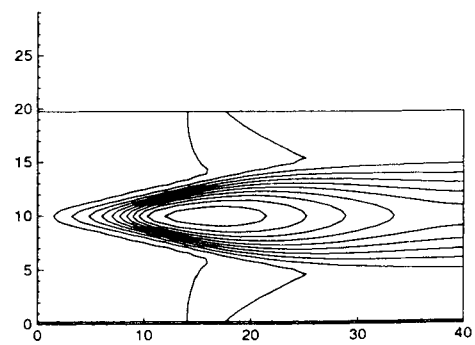

Figure 2. Contours of mean axial velocity as computed using ARSM (contour levels from −0·1 to 0·9 in intervals of 0·1)

We note that for the K–ε model with a value of $\delta = 0{\cdot}13$ (equivalent to the value for the ARSM results shown here) the minimum velocity along the vortex centreline was approximately 0·35 (thus breakdown had not occurred). In addition, the maximum velocities within the bubble (in the negative x-direction) for the laminar calculations approached 0·55.

The final mean flow quantity to be examined is the axial vorticity. In Figures 3(a) and 3(b) the differences in the vorticity distribution between turbulent breakdown (computed using the ARSM) and laminar breakdown are contrasted. The inflow distribution is identical in each case. However, the decay in vorticity as a function of streamwise distance takes place much more rapidly for the laminar case. In addition, the vorticity distribution is much more complicated within the laminar bubble and regions of negative vorticity exist for the laminar case only (indicated by the broken contours). Downstream of the breakdown the levels of vorticity in the vortex core are approximately three times higher for laminar breakdown than for turbulent breakdown. This indicates that subsequent breakdown bubbles, which are often observed downstream of an initial laminar breakdown bubble, are much less likely to occur for the turbulent case.

The spatial distribution of turbulence kinetic energy for the ARSM is shown in Figure 4(a). As stated in the previous section, the maximum (fixed) level at inflow is 0·1 and occurs at the vortex centreline. The figure reveals a rapid decrease in the kinetic energy as the vortex evolves in the streamwise direction. A local minimum is reached at a point just upstream of the breakdown. Within the breakdown region a local maximum in turbulence kinetic energy develops, the location of which corresponds to the outer portion of the toroidal region of the breakdown (as revealed by the streamlines

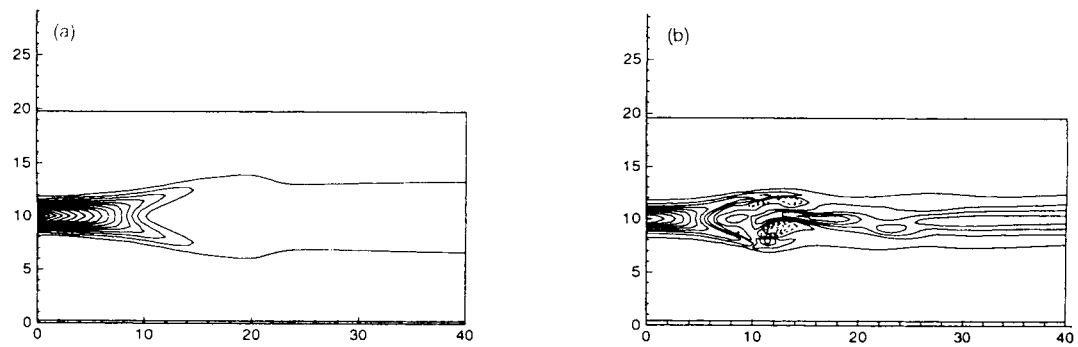

Figure 3. Contours of axial vorticity: (a) ARSM (contour levels from 0·1 to 1·9 in intervals of 0·1); (b) laminar breakdown (contour levels from −0·7 to 1·9 in intervals of 0·2)

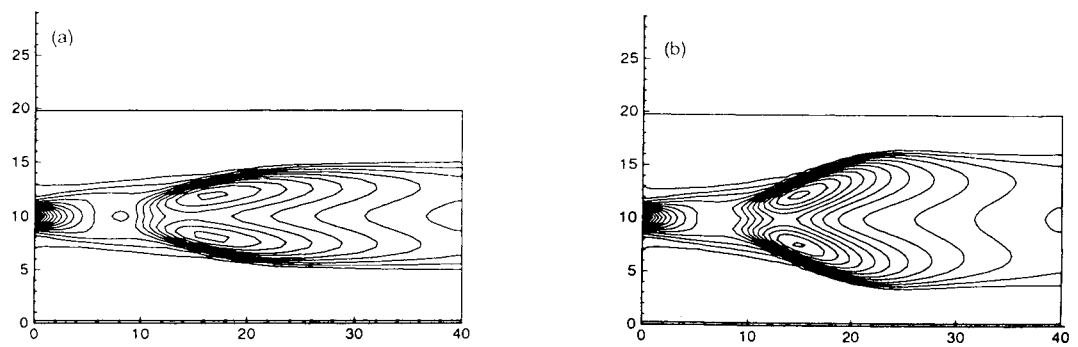

Figure 4. Contours of constant turbulence kinetic energy: (a) ARSM (contour levels from 0·01 to 0·09 in intervals of 0·005); (b) K–ε model (contour levels from 0·1 to 0·09 in intervals of 0·005)

in Figure 1(a). Downstream of the breakdown the kinetic energy distribution is such that the maximum occurs at a radial location off the vortex centreline. Thus the turbulence is damped near the centre of the vortex core. We note that qualitatively similar distribution was also implemented as an inflow boundary condition in the present study. The results of that calculation showed no significant differences in the structure of the resulting breakdown region (compared with the results presented herein using the Gaussian distribution of turbulence kinetic energy). Contours of turbulence kinetic energy for the K–ε model are shown in Figure 4(b). The primary differences between the K–ε and ARSM appear downstream of the bubble. For instance, the radial gradients in turbulence kinetic energy are greater for the ARSM than for the K–ε model.

Contours of constant turbulence dissipation rate ε are shown in Figure 5 for the ARSM. The distribution of these contours corresponds very closely to those for the turbulence kinetic energy. The dissipation rate is high near the inflow region. (For clarity, contours above level 0·01, near the inflow, have been excluded.) The dissipation rate decreases continuously, reaching a local minimum near the point of the onset of breakdown. A maximum in the dissipation rate also occurs within the toroidal recirculation cell, corresponding to the maximum in the turbulence kinetic energy as mentioned in regard to Figure 4(a). Downstream of the breakdown region the dissipation rate is quite low, corresponding to the continual decrease in turbulence kinetic energy. Results from the K–ε model follow these general trends.

Shown in Figure 6 are contributions to the rate of change of turbulence kinetic energy due to the production and dissipation terms in equation (9). These quantities are plotted as a function of streamwise location. Volume integrals were evaluated at each of the 74 grid cell locations and over all the cells in the corresponding y–z plane. The results at each x-station were then normalized by the respective volume (i.e. $400\Delta x$). Thus the results are to be interpreted as mean rates of change per unit volume. The figure highlights the large increase in the production of turbulence kinetic energy over the region of the bubble ($10 \leqslant x \leqslant 25$). Corresponding to this increase is a slight increase in the dissipation, somewhat tempering the overall increases in turbulence kinetic energy. Downstream of the bubble a gradual decrease in production and dissipation takes place.

The ARSM formally constitutes a two-equation turbulence model and employs the concept of an eddy viscosity for the diffusion terms in the transport equations for K and ε. In this sense it is useful to look at the distribution of the turbulent viscosity ($C_\mu K^2/\varepsilon$) and C_μ, where

$$C_\mu = \frac{6(1-\eta^2)\alpha_1 g(2-C_3)}{3+\eta^2+6\zeta^2\eta^2+6\zeta^2} \tag{15}$$

and the variables η and ζ are as previously defined. Figure 7(a) reveals that for the ARSM the turbulent

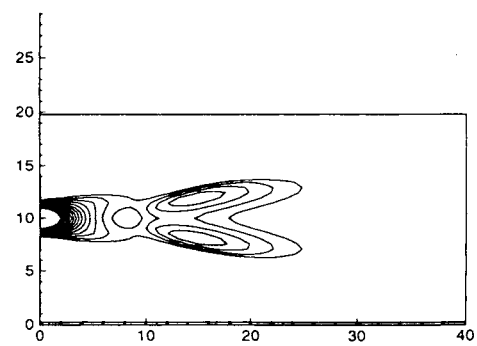

Figure 5. Contours of turbulence dissipation rate computed using ARSM (contour levels from 0·002 to 0·01 in intervals of 0·0005)

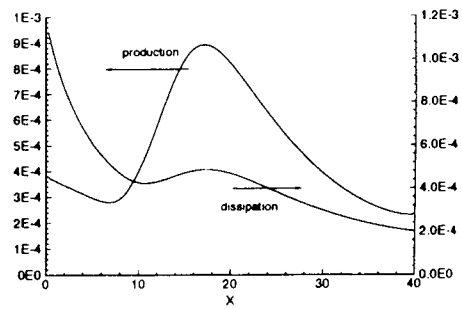

Figure 6. Variation in integrated rate of change of production and dissipation of turbulence kinetic energy with axial location

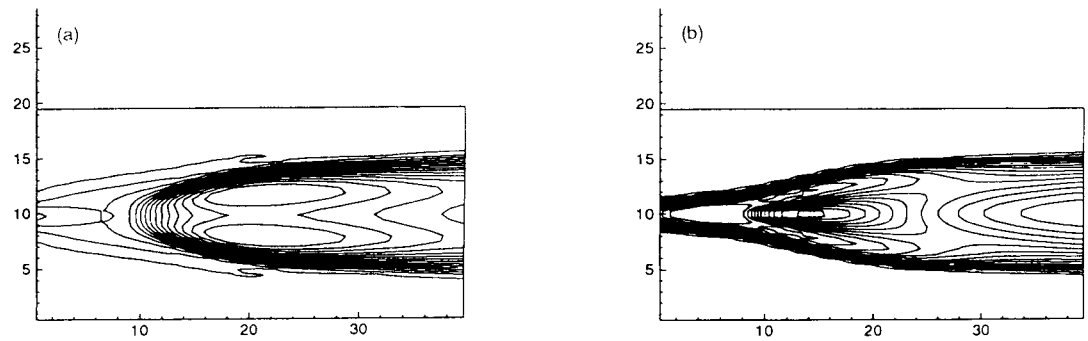

Figure 7. (a) Contours of constant turbulent viscosity $\nu_t = C_\mu K^2/\varepsilon$ for ARSM (contour levels from 0·01 to 0·08 in intervals of 0·005). (b) Contours of constant C_μ for ARSM (contours from 0·04 to 0·11 in intervals of 0·005)

viscosity varies by a factor of approximately eight over the flow field. Upstream of the breakdown ν_t remains nearly constant (as a function of x). However, the level of ν_t begins to rapidly increase immediately downstream of the (initial) stagnation point. The maximum levels occur over a region corresponding to the outer envelope of the bubble, with levels nearly as high over the entire interior bubble region. Downstream of the bubble the levels of ν_t slowly decrease with respect to increasing x, with a local minimum in ν_t developing along the vortex centreline. Thus the formation of the bubble generates high levels of ν_t and these levels persist for some distance downstream of the breakdown.

Shown in Figure 7(b) is the spatial variation of C_μ for the ARSM. Note here that C_μ is in general minimum along the vortex centreline, reaching maximum values outside the vortex core. This is because η, which is directly related to the strain rate tensor, appears in the numerator of C_μ, while ζ, related to the rotation rate, appears only in the denominator. Thus near the vortex centreline, where the flow approaches a solid body rotation, the strain rate becomes small and the rotation rate becomes large. These trends are reversed outside the vortex core. Recall that in the K–ε model the value of C_μ is taken as a constant, typically 0·09. Thus in this manner the ARSM provides a means of sensitizing the calculations to the effects of rotation through the coefficient C_μ. However, within the breakdown bubble itself the value of C_μ is increased relative to the levels near the bubble envelope. In essence, a local minimum in C_μ is defined by the region surrounding the bubble envelope. However, levels within the bubble remain below those far outside the core. Downstream of the bubble the distribution mirrors that occurring upstream of the breakdown, as would be expected (albeit with an expansion in the radial direction).

5. CONCLUSIONS

Numerical solutions for turbulent vortex breakdown were obtained using two different turbulence models: (1) an algebraic Reynolds stress model and (2) a k–ε model. For each model, results revealed the formation of a single, nearly symmetric recirculation region. A primary difference between the results was the level of freestream deceleration required to initiate breakdown. The minimum required value of the deceleration parameter δ was 0·13 for the ARSM and 0·21 for the K–ε model. A possible explanation for this concerns the excessive levels of turbulent diffusion inherent in linear two-equation turbulence models. In addition, the ARSM produced a bubble with a significantly greater L/D ratio. These results were contrasted with (present and previous) calculations for laminar bubble-type breakdown in which a complicated multicell internal structure resulted.

The role of stability in the vortex breakdown process has long been debated. The above calculations support the idea that although stability is probably not important in the initiation of breakdown, stability processes may play an important role in determining the resultant internal structure of the breakdown bubble. In the process of attaining the state shown in Figure 1(c), the laminar bubble passes through a state whose structure is very similar to that of turbulent breakdown (i.e. a single toroidal recirculation zone). The idea is that instabilities then render the single-cell structure as a temporary state. For the turbulent cases, transport processes may tend to damp out these disturbances. The authors plan to study this subject in more detail.

ACKNOWLEDGEMENTS

One of us (R.E.S.) would like to acknowledge the NASA JOVE programme and the Theoretical Flow Physics Branch at NASA Langley Research Center for providing the necessary support to complete this work.

REFERENCES

1. N. Syred and J. M. Beer, 'Combustion in swirling flows: a review', *Combust. Flame*, **23**, 143–201 (1974).
2. M. G. Hall, 'Vortex breakdown', *Ann. Rev. Fluid Mech.*, **4**, 195–218 (1972).
3. S. Leibovich, 'The structure of vortex breakdown', *Ann. Rev. Fluid Mech.*, **10**, 221–246 (1978).
4. T. Sarpkaya, 'On stationary and travelling vortex breakdowns', *J. Fluid Mech.*, **53**, 545–559 (1971).
5. J. H. Faler and S. Leibovich, 'Disrupted states of vortex flow and vortex breakdown', *Phys. Fluids*, **20**, 1385–1400 (1977).
6. J. J. Miau, R. C. Chang, J. H. Chou and C. K. Lin, 'Nonuniform motion of leading-edge vortex breakdown on ramp pitching delta wings', *AIAA J.*, **30**, 1691–1702 (1992).
7. J. H. Faler and S. Leibovich, 'An experimental map of the internal structure of vortex breakdown', *J. Fluid. Mech.*, **86**, 313–335 (1978).
8. G. Brücker, 'Study of vortex breakdown by particle tracking velocimetry (PTV). Part 2: Spiral-type vortex breakdown', *Exp. Fluids*, **14**, 133–139 (1993).
9. H. Altgeld, W. P. Jones and J. Willhelmi 'Velocity measurements in a confined swirl driven recirculating flow', *Exp. Fluids*, **1**, 73–78 (1983).
10. M. P. Escudier and J. J. Keller, 'Recirculation in swirling flow: a manifestation of vortex breakdown', *AIAA J.*, **23**, 111–116 (1985).
11. W. L. H. Hallett and D. J. Toews, 'The effects of inlet conditions and expansion ratio on the onset of flow reversal in swirling flow in a sudden expansion', *Exp. Fluids*, **5**, 129–133 (1987).
12. R. M. Kopecky and K. E. Torrance, 'Initiation and structure of axisymmetric eddies in a rotating stream', *Comput. Fluids*, **1**, 289–300 (1973).
13. W. J. Grabowski and S. A. Berger, 'Solutions of the Navier–Stokes equations for vortex breakdown', *J. Fluid Mech.*, **75**, 525–544 (1976).
14. M. Breuer and D. Hänel, 'Solution of 3-D incompressible Navier-Stokes equations for the simulation of vortex breakdown', *Notes on Numerical Fluid Mechanics*, Vieweg, Braunschweig, 1989, pp.
15. M. Breuer and D. Hänel. 'A dual time-stepping method for 3-D. Viscous, incompressible vortex flows', *Comput. Fluids*, **22**, 467–484 (1993).
16. R. E. Spall, T. B. Gatski and R. L. Ash, 'The structure and dynamics of bubble-type vortex breakdown', *Proc. R. Soc. Lond. A*, **429**, 613–637 (1990).

17. R. E. Spall and T. B. Gatski, 'A computational study of the topology of vortex breakdown', *Proc. R. Soc. Lond. A.* **435**, 321–337 (1991).
18. S. Menne, 'Simulation of vortex breakdown in tubes', *AIAA Paper 88-3575*, 1988.
19. E. Krause, 'The solution to the problem of vortex breakdown', in *Lecture Notes in Physics*, Vol. 377, Springer, Berlin, 1990, pp. 35–39.
20. R. E. Spall, T. B. Gatski and G. Kandare, 'Qualitative aspects of three-dimensional vortex breakdown', *Int. Video J. Eng. Res.*, **2**, 63–72 (1992).
21. D. L. Rhode, D. G. Lilley and D. K. McLauglin, 'On the prediction of swirling flowfields found in axisymmetric combustor geometries', *J. Fluids Eng.*, **104**, 378–384 (1982).
22. S. Hogg and M. A. Leschziner, 'Computation of highly swirling confined flow with a Reynolds stress turbulence model', *AIAA J.*, **27**, 57–63 (1989).
23. W. P. Jones and A. Pascau, 'Calculation of confined swirling flows with a second moment closure', *J. Fluids Eng.*, **111**, 248–255 (1989).
24. S.-H. Chuang, H.-C. Lin, M.-H. Chen and J.-F. Jan, 'Theoretical investigation of combustor characteristics in ram-jet dump combustor with side-inlet', *Int. j. numer. methods fluids*, **15**, 1197–1212 (1992).
25. T. B. Gatski and C. Speziale, 'On explicit algebraic stress models for complex turbulent flows', *J. Fluid Mech.*, **254**, 59–78 (1993).
26. T. B. Gatski, C. E. Grosch and M. R. Rose, 'The numerical solution of Navier–Stokes equations for three-dimensional unsteady, incompressible flows by compact schemes', *J. Comput Phys.*, **82**, 298–329 (1989).
27. C. G. Speziale, S. Sarkar and T. B. Gatski, 'Modeling the pressure-strain correlation of turbulence: an invariant dynamical systems approach', *J. Fluid Mech.*, **227**, 245–272 (1991).
28. N. A. Chigier and V. R. Corsiglia, 'Wind-tunnel studies of wing wake turbulence', *AIAA Paper 72-41*, 1972.
29. A. J. Bilanin, M. E. Teske, C. Donaldson and G. G. Williamson, 'Vortex interactions and decay in aircraft wakes', *NASA CR-2870*, 1977.
30. R. E. Spall, T. B. Gatski and C. E. Grosch, 'A criterion for vortex breakdown', *Phys. Fluids*, **30**, 3434–3440 (1987).